Radiation Characteristics of Cranial Leaky Lamb Waves

Matteo Mazzotti, Eetu Kohtanen, Alper Erturk, and Massimo Ruzzene

***Abstract*— We numerically and experimentally investigate the dispersion properties of leaky Lamb waves in the cranial bone. Cranial Lamb waves leak energy from the skull into the brain when propagating at speeds higher than the speed of sound in the surrounding fluid. The understanding of their radiation mechanism is significantly complicated by the geometric and mechanical characteristics of the cortical tables and the trabecular bone (diploë). Toward such understanding, we here analyze the sub-1.0 MHz radiation angle dispersion spectrum of porous bone phantoms and parietal bone geometries obtained from μCT scans. Our numerical results show that, when diploic pores are physically modeled, leakage angles computed from time transient finite-element analyses correspond to those predicted by an equivalent three-layered fluid-loaded waveguide model. For the bone geometries analyzed, two main leaky branches are observed in the near-field dispersion spectrum: a fast wave radiated at small angles, which is related to the fastest fundamental Lamb mode supported by the cranial bone, and a slower wave radiated at larger angles. This observation is also confirmed by experimental tests carried out on an immersed parietal bone.**

***Index Terms*— Medical signal and image processing, medical tissue characterization, underwater ultrasound, wave propagation.**

I. Introduction

TRANSCRANIAL focused ultrasound (tFUS) has recently opened new avenues for a diverse and minimally invasive set of biomedical applications in brain diagnostics and therapy. Many of these applications take advantage of the brain's coupled physical and electrical nature. For example, pressure waves (ultrasound) are hypothesized to influence neuronal activity via a number of complex electromechanical pathways [1] and have shown success for treatment of essential tremor via tFUS thalamotomy [2]. Higher intensity tFUS could also be employed for the ablation of metastases along the brain periphery. However, the conventional treatment envelope is limited to the center of the brain, and tFUS is often accompanied by high levels of undesired heating in the bone [3]–[5]. Addressing these problems could multiply the medical possibilities offered by ultrasound, possibly creating treatment options for other neurological conditions. While the skull presents a barrier to pressure waves used in conventional ultrasound treatments, waves that exploit the quasi-bidimensional geometry of the cranial bone could, in principle, lead to valuable improvements in ultrasound technology. In this context, recent studies have showcased the potential of skull guided waves for brain diagnostics and therapy. For example, Lamb waves in human skulls have been experimentally and numerically investigated by Estrada *et al.* [6]–[8] and Sugino *et al.* [9]. In a parallel line of work, Firouzi *et al.* [10] and Kang *et al.* [11] have demonstrated that limitations in ultrasound treatment envelope and excessive heating can be addressed through transducer designs that take advantage of efficient mode conversion between bulk waves in fluid and Lamb waves in the bone. Also, Adams *et al.* [12] have proposed a concave array transducer to excite guided waves in a three-layered cranial bone phantom and have numerically simulated wavefronts associated with leaky Lamb waves in the far-field. Other computational studies have modeled the actual bone geometry from CT images to investigate tFUS adaptive focusing [13], to evaluate its effects on ultrasound propagation [14]–[21], diagnose osteoporosis [22], measure bulk wave attenuation [23], [24], and determine the relationship between ultrasonic backscatter and trabecular microstructural variations [25]. However, as pointed out by Estrada *et al.* [7], little is known about the effect of the cranial bone structure on guided wave propagation in the sub-1.0 MHz regime and on how the radiation properties of Lamb waves are consequently altered. In addition, studies showing dispersion diagrams with distinct leaky Lamb wave branches from simulated real bone geometries or experimental tests are, to the best of our knowledge, not available in the existing literature.

This work takes a first step toward filling the above-mentioned gap. To this end, bone phantoms with an inner layer of varying porosity and μCT scanned geometries of real parietal bones are numerically investigated in the sub-1.0 MHz regime to determine their dispersion characteristics in terms of radiation angles. The methods used to compute the dispersion diagrams consist of time-domain FE models of the artificial and real bone geometries immersed in water and

Manuscript received December 1, 2020; accepted February 2, 2021. Date of publication February 5, 2021; date of current version May 25, 2021. This work was supported by the National Science Foundation CMMI Award No. 1933158 on Coupling Skull-Brain Vibroacoustics and Ultrasound Toward Enhanced Imaging, Diagnosis, and Therapy. *(Corresponding author: Matteo Mazzotti.)*

Matteo Mazzotti and Massimo Ruzzene are with the Department of Mechanical Engineering, University of Colorado Boulder, Boulder, CO 80309 USA (e-mail: teomazzotti@gmail.com).

Eetu Kohtanen and Alper Erturk are with the Department of Mechanical Engineering, Georgia Institute of Technology, Atlanta, GA 30332 USA.

This article has supplementary downloadable material available at https://doi.org/10.1109/TUFFC.2021.3057309, provided by the authors.

Digital Object Identifier 10.1109/TUFFC.2021.3057309

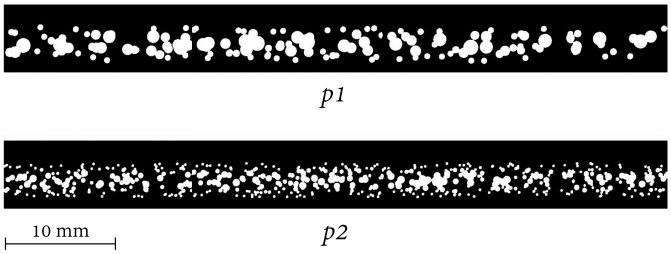

Fig. 1. Bone phantoms $p1$ and $p2$ of 6 mm thickness and mimicked trabecular pores. The average size of the pores of phantom $p1$ is twice that of phantom $p2$.

semi-analytical finite element (SAFE) models with equivalent geometric and material properties. The obtained numerical results are finally corroborated by an experimental test performed on an immersed parietal bone.

II. Bone Geometries and Mechanical Properties

This section describes the geometric and mechanical properties of the bones used in the numerical and experimental analyses of Section III–V. These consist of the two bone phantoms of Fig. 1 and the three parietal bone sections of Fig. 2.

A. Bone Phantoms

The bone phantoms $p1$ and $p2$ in Fig. 1 were generated using a Boolean subtraction algorithm similar to that presented by Hosokawa [19]. The algorithm creates a random spatial distribution of circular pores whose diameters are randomized between specified lower and upper bounds. Larger pores are biased toward the middle thickness of the bone. Both geometries were initiated from primitive layered plates in which the thicknesses of the upper cortical layer, diploë, and lower cortical layer were set to 2, 3, and 1 mm, respectively. Before the Boolean subtraction was conducted, each circular pore was spatially allocated in such a way that its center remained confined within the diploë. Two different porosity scenarios were created by selecting pore diameters for the phantom $p1$ that are twice the size of those in $p2$.

B. μCT Scan Images of Parietal Bone Samples

The microcomputed tomographic (μCT) scan images of Fig. 2 were obtained for two different skull specimens. For the first specimen (60-year-old male, as shown in Fig. 2(a)), a 94 mm × 43 mm rectangular parietal cut was first obtained and then scanned using a Scanco Medical μCT 50 scanner at 100-μm resolution. The μCT scans were then employed to construct a 3-D geometry through the Materialise Mimics software [26], from which a sagittal and a coronal section were extracted. These are indicated as $s1$ and $s2$ in Fig. 2(a) and (b), respectively. A 30 mm × 90 mm parietal cut was obtained from a second specimen (87-year-old male, as shown in Fig. 2(c)) and scanned using the same methodology described above. From the μCT scan model, the sagittal section $s3$ was then extracted, as shown in Fig. 2(c) and (d).

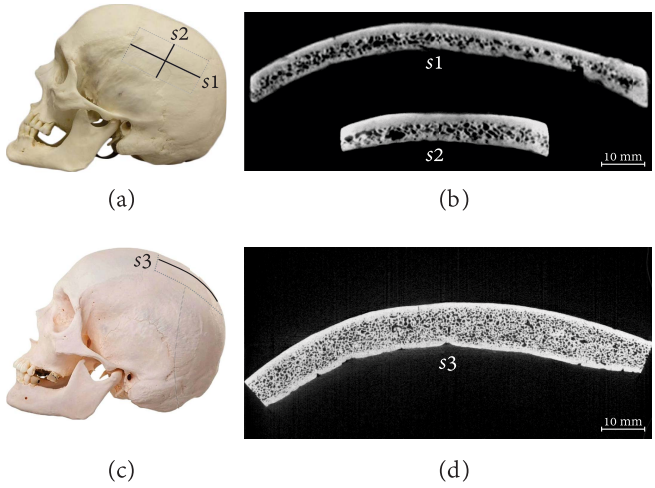

Fig. 2. (a) First human skull specimen with a parietal bone cut and μCT images of (b) sections $s1$ and $s2$. (c) Second human skull specimen with a parietal bone cut and a μCT image of (d) section $s3$.

C. Mechanical Properties

The mechanical properties of the parietal sections $s1$ and $s2$ (see Fig. 2(a) and (b)) are not available and were, therefore, estimated from those of the parietal location P12 provided by Peterson and Dechow [27], which were obtained from ultrasonic transmission analyses performed on degassed cortical bone samples. The same properties were also used to analyze the two bone phantoms $p1$ and $p2$. Following [6] and [7], the mechanical behavior of the diploë for the bone phantoms $p1$ and $p2$ and sections $s1$ and $s2$ was assumed to be equivalent isotropic. All the above mentioned mechanical properties are listed in Table I.

The equivalent isotropic mechanical properties for the cortical and trabecular bone of the parietal section $s3$ (see Fig. 2(c) and (d)) are also reported in Table I. These were experimentally estimated by Kohtanen *et al.* [28] by means of optimization procedures aimed at matching finite-element (FE) simulations with vibration experiments.

Also, for the purpose of this work, the effect of material attenuation was neglected. The rationale behind this assumption is that the effect of bone hysteresis and internal scattering by microporosity on the radiation characteristics of cranial leaky Lamb waves is considered small compared to the effect of the fluid loading.

III. Dispersion Analysis for the Cranial Bone

This section describes the SAFE approach [29]–[31] employed to predict the frequency-dependent wavenumbers and radiation angles of leaky Lamb waves propagating in the cranial bone. Specifically, the model is used in Sections IV and V to compare the radiation angles obtained from time transient simulation and experimental pressure field measurements with those predicted by a plate theory. In the SAFE method, the cranial bone is idealized as an unbounded plate loaded on the top and bottom surfaces with a water half-space. This approach has proven sufficiently accurate in predicting the propagation characteristics of cranial Lamb waves in human skulls [6]–[9]

TABLE I

MATERIAL CONSTANTS FOR THE BONE GEOMETRIES OF Figs. 1 AND 2. THE MATERIAL DIRECTIONS ARE DEFINED WITH RESPECT TO THE CARTESIAN FRAME OF REFERENCE OF Figs. 3–9

Section	Layer	ρ [kg/m^3]	E_1 [GPa]	E_2 [GPa]	E_3 [GPa]	G_{12} [GPa]	G_{13} [GPa]	G_{23} [GPa]	ν_{12} -	ν_{13} -	ν_{23} -
$p1$, $p2$, $s1$, $s2$	cortical [27]	1824	21.50	13.10	12.80	6.90	5.40	4.60	0.39	0.31	0.48
	trabecular	1100	5.00	5.00	5.00	1.79	1.79	1.79	0.40	0.40	0.40
$s3$	cortical [28]	1944	14.70	14.70	14.70	5.88	5.88	5.88	0.25	0.25	0.25
	trabecular [28]	1211	5.70	5.70	5.70	2.59	2.59	2.59	0.10	0.10	0.10

TABLE II

AVERAGE CORTICAL AND TRABECULAR THICKNESSES EMPLOYED IN THE ANALYSES OF SECTIONS IV AND V

Geometry	Inner cortical (t_i) [mm]	Trabecular (t_d) [mm]	Outer cortical (t_o) [mm]
$p1$	1.786	1.824	2.389
$p2$	1.672	2.089	2.239
$s1$ (scan area 1)	1.263	2.163	2.394
$s1$ (scan area 2)	2.021	1.434	2.414
$s2$	1.483	2.145	2.373
$s3$	1.382	7.218	1.546

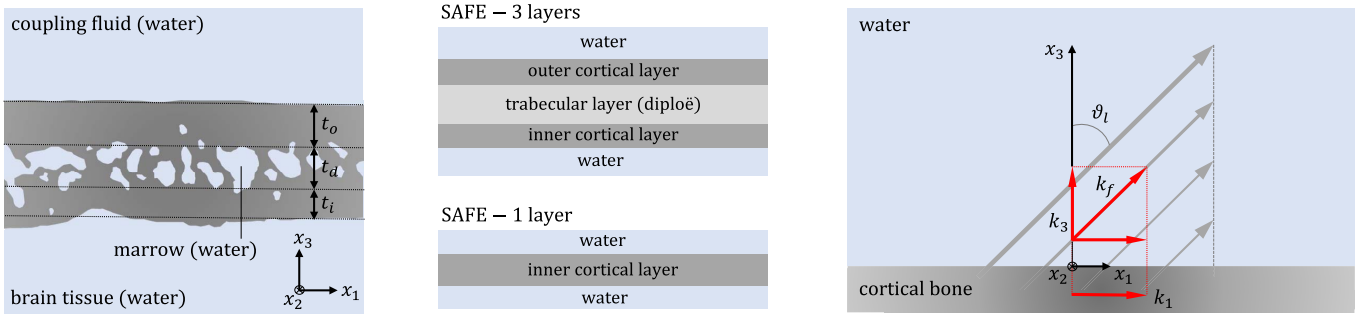

(a) (b) (c)

Fig. 3. (a) Immersed bone geometry with equivalent inner cortical (t_i), trabecular (t_d), and outer cortical (t_o) thicknesses. (b) SAFE plate models based on three and one layer. (c) Schematic of the radiation mechanism.

and in 3-D printed skull phantoms [32]. The effects of the trabecular bone and cranial marrow are considered by the two modeling approaches shown in Fig. 3(b). In the first approach, the cranial bone is idealized as a three-layered plate. With reference to Fig. 3(a), the three different layers correspond to the outer cortical table, the diploë, and the inner cortical table. Their equivalent thicknesses are indicated as t_o, t_d, and t_i, respectively. For each bone geometry of Section II, the equivalent thicknesses are reported in Table II and were obtained by averaging the geometry shown in Fig. 3(a). In the second approach, the inner cortical layer of thickness t_i is analyzed independently as a plate loaded by water on the top (cranial bone marrow) and bottom (soft brain tissue). This simplified approach is used to test the performance of the full multilayered model for bone geometries in which the scattering effect associated with the diploë confines the wave motion to the proximity of the cortical layers [7].

With reference to Fig. 3(c), the SAFE approach discretizes a through-thickness segment of the plate into 1-D finite elements. At any nodal coordinate along the x_3-direction, the 3-D displacement field $\mathbf{u}(x_3) = \{u_1(x_3), u_2(x_3), u_3(x_3)\}^{\mathrm{T}}$ is interpolated using quadratic polynomial shape functions and is harmonically modulated in time and space as $\exp[i(k_1 x_1 - 2\pi f t)]$, where f (Hz) denotes the frequency and k_1 (rad/m) the Lamb wavenumber. The through-the-thickness discretization produces a sixth-order polynomial eigenvalue problem of the form

$$\left[\sum_{i=0}^{6} \gamma^i(f)\mathbf{A}_i(f)\right]\mathbf{U}(f) = \mathbf{0}. \tag{1}$$

The detailed derivation of (1) and the operators $\mathbf{A}_i(f)$ ($i = 0, \ldots, 6$) are given in the Appendix. The eigenvalues $\gamma(f)$ in (1) can be computed by linearizing the system in state space and applying standard linear eigenvalue solvers. The complex Lamb wavenumbers are obtained for an assigned frequency f as $k_1(f) = k_f(f)[\gamma(f) + \gamma^{-1}(f)]/2$, where $k_f(f) = 2\pi f/c_f$ is the fluid bulk wavenumber (see Fig. 3(c)) and c_f the fluid phase speed. Using the generalized Snell's law (see Fig. 3(c)), the associated radiation angles $\vartheta_l(k(f))$ can finally be obtained from the relation

$$\vartheta_l(f) = \sin^{-1}\left[\frac{\mathrm{Re}(k_1(f))}{k_f(f)}\right] = \sin^{-1}\left[\frac{\mathrm{Re}\left(\gamma(f) + \gamma^{-1}(f)\right)}{2}\right]. \tag{2}$$

IV. Numerical Simulations

The numerical study of the radiation characteristics of cranial Lamb waves by means of FE time transient simulations and the SAFE modeling approaches presented in Section III is presented next. For each geometry of Section II, a qualitative discussion is also provided in terms of computed (FE) versus predicted (SAFE) radiation angles dispersion diagrams. All the analyses were carried out under the assumption of 2-D plane strain conditions. Although this assumption does not account for the curvature of the skull in the (x_2, x_3)-plane, it is noted that such effects were found to be negligible due to the small ratio between the typical skull thickness and curvature radius [7].

A. Time Transient Finite-Element Analysis

Leaky wave radiation angles for the bone geometries of Section II-B were obtained from time transient simulations performed in COMSOL Multiphysics 5.4 [33]. Similar to the assumptions made by Pinton *et al.* [24], the marrow within the trabecular bone was modeled as water (density $\rho_f = 1000$ kg/m^3 and phase speed $c_f = 1480$ m/s), while the material properties assumed for the cortical and trabecular bone are given in Table I. The material directions (1, 2, 3) used in Table I are defined with respect to the Cartesian frame of reference of each scan area in Figs. 3–9.

In all the simulations, the cranial bone geometries are considered to be immersed in water (see Fig. 3(a)), which is used to model the external coupling fluid and to mimic the soft brain tissue. The transient source is applied at a single point located on the outer cortical table and corresponds to a one-and-a-half cycle tone burst with a center frequency $f_c = 500$ kHz. The numerical convergence of the FE models was ensured by setting the maximum element size $l_{\max}$ equal to the shortest shear wave wavelength as defined by the classical rule of thumb for quadratic elements $l_{\max} = c_{s,\min}/(7f_0)$, with $f_0 = 1.0$ MHz. The slowest shear wave speed was obtained from Table I as $c_{s,\min} = (\min G_{ij}/\rho)^{1/2}$. Similarly, the maximum step size for the finite difference-based time marching scheme was assumed equal to $\Delta t_{\max} = 0.1/(7f_0)$. The total duration of the simulated transient phase was set to 300 μs for each analysis. Finally, to limit the size of the model, absorbing boundary conditions were applied to the external truncated boundaries of the acoustic domain.

B. Radiation Angle Dispersion Diagrams From Synthetic Waveforms

The radiation characteristics of leaky Lamb waves are estimated from the computed pressure field amplitude in the acoustic near-field region below the inner cortical layers. The extension of each scan area is outlined in the modeling plane x_1x_3 of Figs. 4–8 with dashed lines. The pressure field recorded within each region was used to construct a 3-D waveform array $p(t, x_1, x_3)$. Each array was then Fourier-transformed in the temporal frequency f and spatial wavenumbers k_1, k_3 (see Fig. 3(c)), i.e., $\hat{p}(f, k_1, k_3)$. To avoid side lobes effects in the Fourier spectra, a cosine-tapered (Tukey) window was applied on the spatial and temporal signals. The ratio of the length of the tapered section to the total length of the window was chosen as 0.85.

With reference to Fig. 3(c), the frequency versus radiation angle $(f - \vartheta_l(f))$ dispersion diagram within a scanned acoustic region was obtained by evaluating the spectral amplitude $|\hat{p}(f, k_1, k_3)|$ at any coordinate $\tan^{-1}[\mathrm{Re}(k_1(f))/\mathrm{Re}(k_3(f))]$ for a given frequency abscissa f. For visualization purposes, each spectrum was normalized frequencywise with respect to the maximum amplitude of $|\hat{p}(f, k_1, k_3)|$. The radiation angle dispersion diagrams define the main directions (measured with respect to the average normal to the fluid-bone interface) along which the mechanical energy flows from the bone into the surrounding water. In Section IV-C, such diagrams are compared with the corresponding ones obtained from (2) for each bone geometry.

C. Results and Discussion

In this section, the radiation angle dispersion diagrams of the bone phantoms and μCT-scanned parietal geometries of Section II are discussed by comparing the results obtained from the time-transient FE analyses and the SAFE models. In all the dispersion spectra analyzed in the following, only Lamb modes with spatial attenuation $\mathrm{Im}(k_1(f)) < 1000$ np/m are considered.

1) Bone Phantoms p1 and p2: We first analyze the wave and radiation behavior in the bone phantoms $p1$ and $p2$, whose results are shown in Figs. 4 and 5, respectively. As observed from the snapshots of the pressure field in Figs. 4(a) and 5(a), two distinct wavefronts are clearly present in the fluid domain above and below the outer and inner cortical layers, respectively. The semi-circular wavefronts of high-pressure amplitude correspond to the direct wave generated by the point source, which is located at the outer fluid-bone interface and marked with a filled circle. The low-amplitude pressure wavefront generated by leaky Lamb waves is located in front of the direct waves, along the wave propagation direction (positive x_1-direction). In order to analyze the main radiation angles of the different leaky guided wave modes excited in the bone, the procedure described in Section IV-B was carried out on the pressure field $p(t, x_1, x_3)$ recorded within each scanned area (indicated with dashed rectangular boxes in Figs. 4(a) and 5(a)). The corresponding normalized radiation angle dispersion diagrams for the phantoms $p1$ and $p2$ are reported in Figs. 4(b) and 5(b), respectively. These diagrams also display the dispersion curves computed with the SAFE method using the three-layer (continuous lines) and one-layer (hollow circles) modeling approaches described in Section III. As it can be noted, the main propagation branch is located at $\vartheta_l \approx 25°$ only (as measured with respect to the x_3-axis). SAFE calculations reveal that this branch corresponds to the fundamental Lamb wave mode with a through-the-thickness displacement polarization that is dominant along the wave propagation direction. For the three-layer SAFE model (superscript $(\cdot)^{(3L)}$), such mode is labeled as $m_1^{(3L)}$, whereas, for the one-layer SAFE model (superscript $(\cdot)^{(1L)}$)

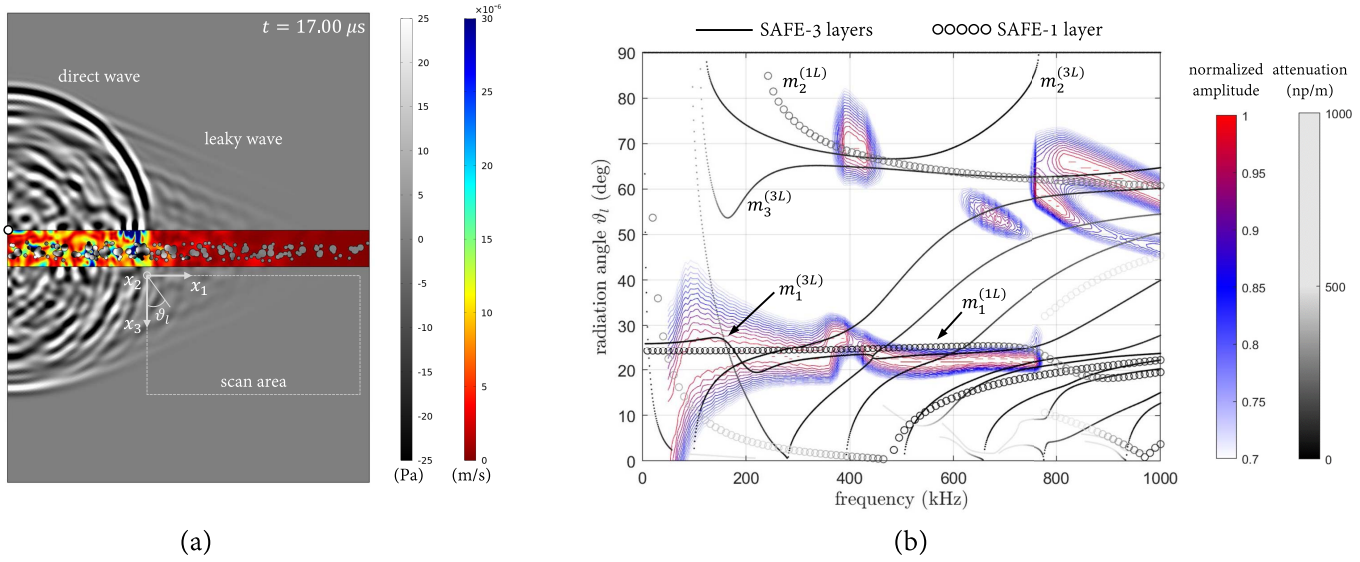

Fig. 4. Results for the bone phantom *p*1 of Fig. 1. (a) Time snapshot of the velocity and pressure fields. (b) Radiation angle dispersion diagram from time transient FE and SAFE analyses.

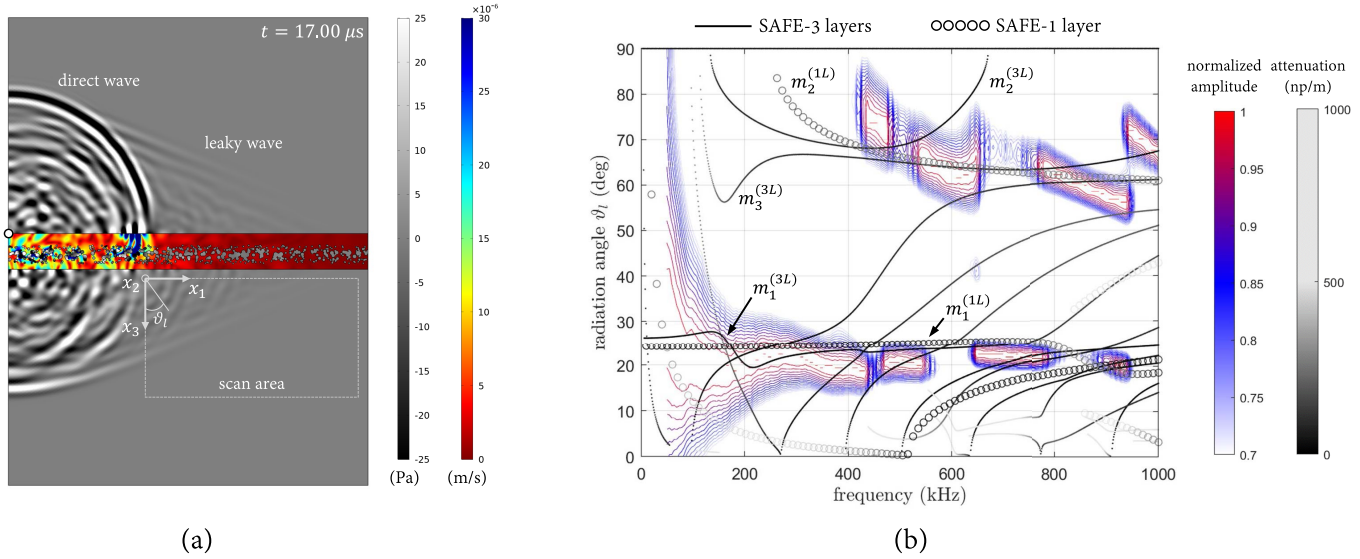

Fig. 5. Results for the bone phantom *p*2 of Fig. 1. (a) Time snapshot of the velocity and pressure fields. (b) Radiation angle dispersion diagram from time transient FE and SAFE analyses.

is indicated as $m_1^{(1L)}$. It is interesting to note that the one-layer SAFE model was capable to predict the dispersive behavior of this mode with a maximum error of about 5°. At frequencies above 400 kHz, radiation also occurs for both phantoms in the range $\vartheta_l \in [50, 80]°$. Since leaky Lamb modes with higher radiation angles have smaller wavelengths, they are expected to be affected more by local variations of the cortical thickness and the diploic pores. Consequently, their radiation angle dispersion branches are expected to exhibit larger variations compared with the SAFE predictions. Nonetheless, the radiation angles could still be estimated by the fundamental $m_2^{(3L)}$ and high order $m_3^{(3L)}$ of the three-layer SAFE model and the fundamental mode $m_2^{(1L)}$ of the one-layer SAFE model. Since these modes exhibit a through-the-thickness displacement polarization that is dominant along the direction normal to the fluid-bone interface, their attenuation is larger than that of modes $m_1^{(3L)}$ and $m_1^{(1L)}$ due to the higher structure-to-fluid coupling strength. This behavior is represented in the SAFE dispersion curves of Figs. 4(b) and 5(b) by means of a gray color gradient.

As a general observation, it can be inferred that the capability of the one-layer SAFE model to predict the radiation angle dispersion curves of the fundamental Lamb wave modes can be attributed to the large diploic pores, whose scattering effect essentially confines most of the guided wave motion within the two cortical layers. It should be noted that such an effect can pose some limitations on the use of cranial guided waves since the higher absorption found in the skull would severely attenuate multiple internal reflections.

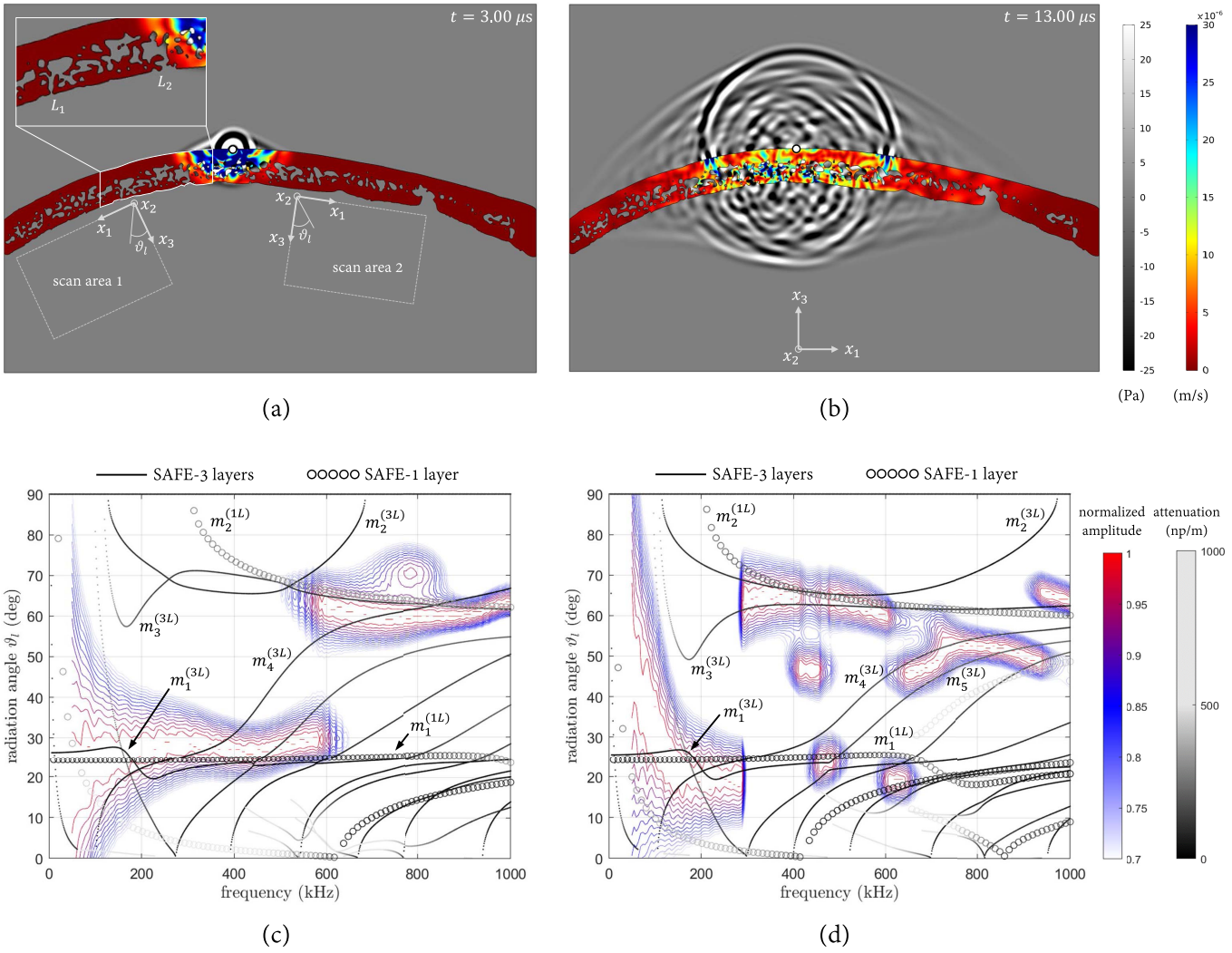

Fig. 6. Results for the parietal section $s1$ of Fig. 2(b). (a)–(b) Different time snapshots of the velocity and pressure fields. (c) Radiation angle dispersion diagram from time transient FE and SAFE analyses for the scan area 1. (d) Radiation angle dispersion diagram from time transient FE and SAFE analyses for the scan area 2.

2) Parietal Sections s1, s2, and s3: The results for the three parietal sections $s1$, $s2$, and $s3$ (see Fig. 2) are reported in Figs. 6–8, respectively. Compared with the bone phantoms $p1$ and $p2$, the cortical bone surfaces of the parietal sections present several structural dishomogeneities. This is particularly evident for the inner left cortical table of section $s1$ (above scan area 1), which presents points of discontinuity (labeled as L_1 and L_2) associated with the diploic channels.

As previously observed for the bone phantoms, the radiation angle dispersion diagram for the scan area 1 of section $s1$ presents a quasi-nondispersive branch in the 100–600 kHz frequency range, corresponding to a leakage angle $\vartheta_l \approx 28°$ (see Fig. 6(c)). A slightly dispersive branch is also observed in the 600–1000 kHz range, which spans the radiation angles $\vartheta_l \in [55, 65]°$. From the inspection of the SAFE results, it can be deduced that also, in this case, the one-layer SAFE model was capable to predict the radiation angles of the two branches with a maximum error of about 5°. Similar considerations also apply for the fundamental mode $m_2^{(1L)}$ and the high-order modes $m_{3,4}^{(3L)}$ in the 600–1000 kHz range.

The results for the scan area 2 of the $s1$ section (see Fig. 6(d)) show a similar scenario in terms of first and second fundamental modes. However, in the 600–950 kHz frequency range, it can be noticed the presence of a dispersion branch that could only be predicted by the three-layer SAFE model. Such branch is encompassed by the high-order modes $m_4^{(3L)}$ and $m_5^{(3L)}$, whose through-the-thickness displacement profiles are mainly polarized along the x_3-direction.

A scenario similar to that of Fig. 6(d) can also be observed for the parietal section $s2$, for which the near-field scan area and corresponding radiation angle dispersion diagram are reported in Fig. 7(a) and (b), respectively. Also, in this case, the branch for the fastest fundamental Lamb mode present in the spectrum is located in the 200–300 kHz frequency range at $\vartheta_l \approx 28°$ and could be predicted by both SAFE modeling approaches (modes $m_1^{(3L)}$ and $m_1^{(1L)}$). Similarly, the slow mode in the 200–600 and 800–1000 kHz ranges could be predicted

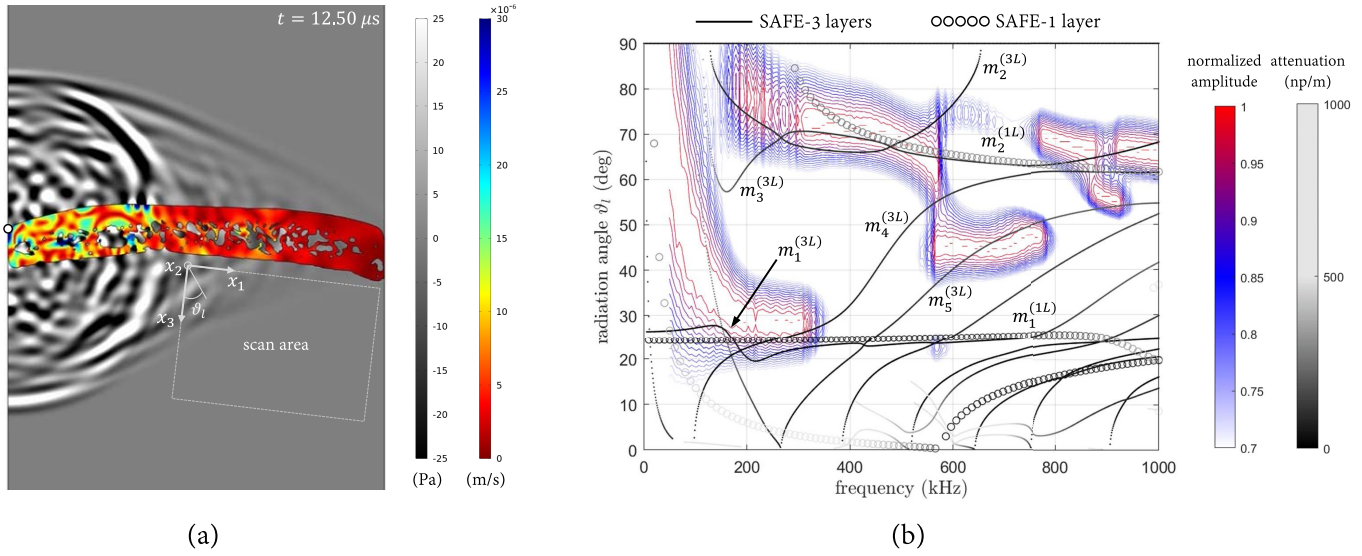

Fig. 7. Results for the parietal section *s*2 of Fig. 2(b). (a) Time snapshot of the velocity and pressure fields. (b) Radiation angle dispersion diagram from time transient FE and SAFE analyses.

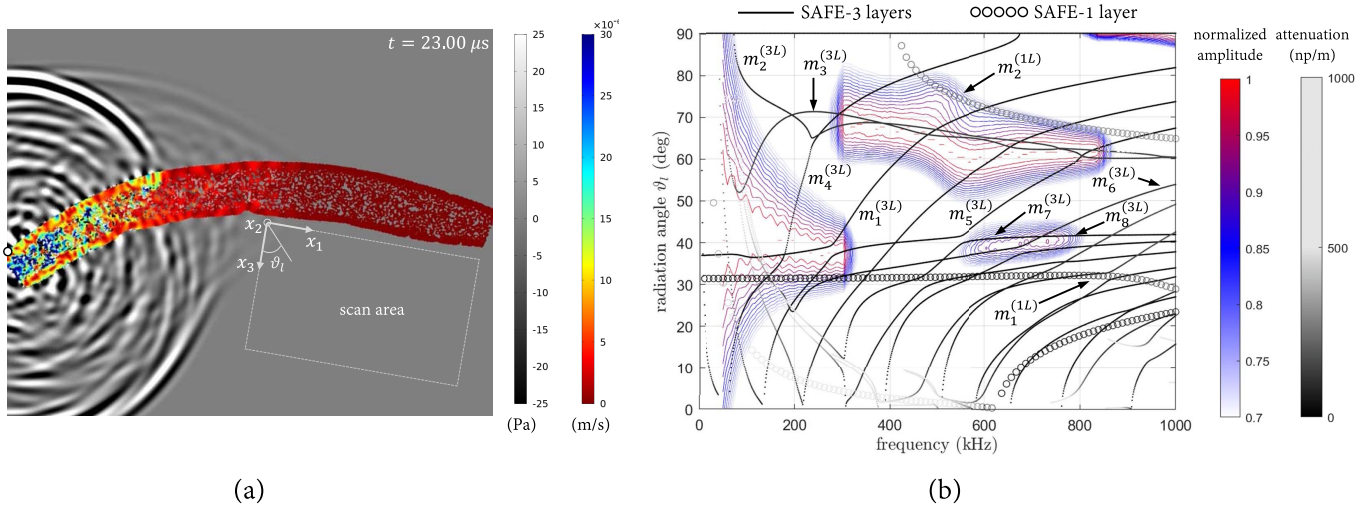

Fig. 8. Results for the parietal section *s*3 of Fig. 2(d). (a) Time snapshot of the velocity and pressure fields. (b) Radiation angle dispersion diagram from time transient FE and SAFE analyses.

by modes $m_3^{(3L)}$ and $m_2^{(1L)}$. However, the leaky mode with angle $\vartheta_l \approx 45°$, which can be observed in the 560–770 kHz range, could only be predicted by the three-layer SAFE model.

The results obtained for the phantoms $p1$ and $p2$ and the parietal sections $s1$ and $s2$ indicate that the SAFE modeling approach based on the use of the inner cortical layer only can lead to accurate results if the fast ($m_1^{(1L)}$) and slow ($m_2^{(1L)}$) fundamental Lamb modes are concerned. This is, however, not the case for the parietal section $s3$. The results for this section are reported in Fig. 8(b) and show that, in this case, the one-layer SAFE model fails in capturing any of the three main radiation branches present in the dispersion spectrum. In particular, it can be observed that the fast fundamental mode ($\vartheta_l \approx 38°$) could only be accurately predicted in the 100–300 kHz range by the three-layer SAFE model (mode $m_1^{(3L)}$). Similarly, the fast branch in the 500–750 kHz range ($\vartheta_l \approx 40°$) is matched by modes $m_{6,7,8}^{(3L)}$, whereas the slow branch in the 300–850 kHz range ($\vartheta_l \in [60, 70]°$) is only captured by modes $m_3^{(3L)}$ and $m_4^{(3L)}$. The poor performance of the one-layer SAFE model is related to the fact that the finely distributed small pores of the parietal section $s3$ result in a lower amount of scattering (or increased energy transmission) between the two cortical layers compared to the parietal sections $s1$ and $s2$. Therefore, the denser trabecular network can sustain a proper guided wave motion, which includes Lamb modes with multiple through-the-thickness wavelengths. Similar conclusions can be found in [34], where high-order Lamb modes have been experimentally and numerically detected in a dry human skull.

A final remark can be made regarding the physical behavior of leaky Lamb waves in the low-frequency regime. In fact, from all the numerical results presented, it appears that, in the

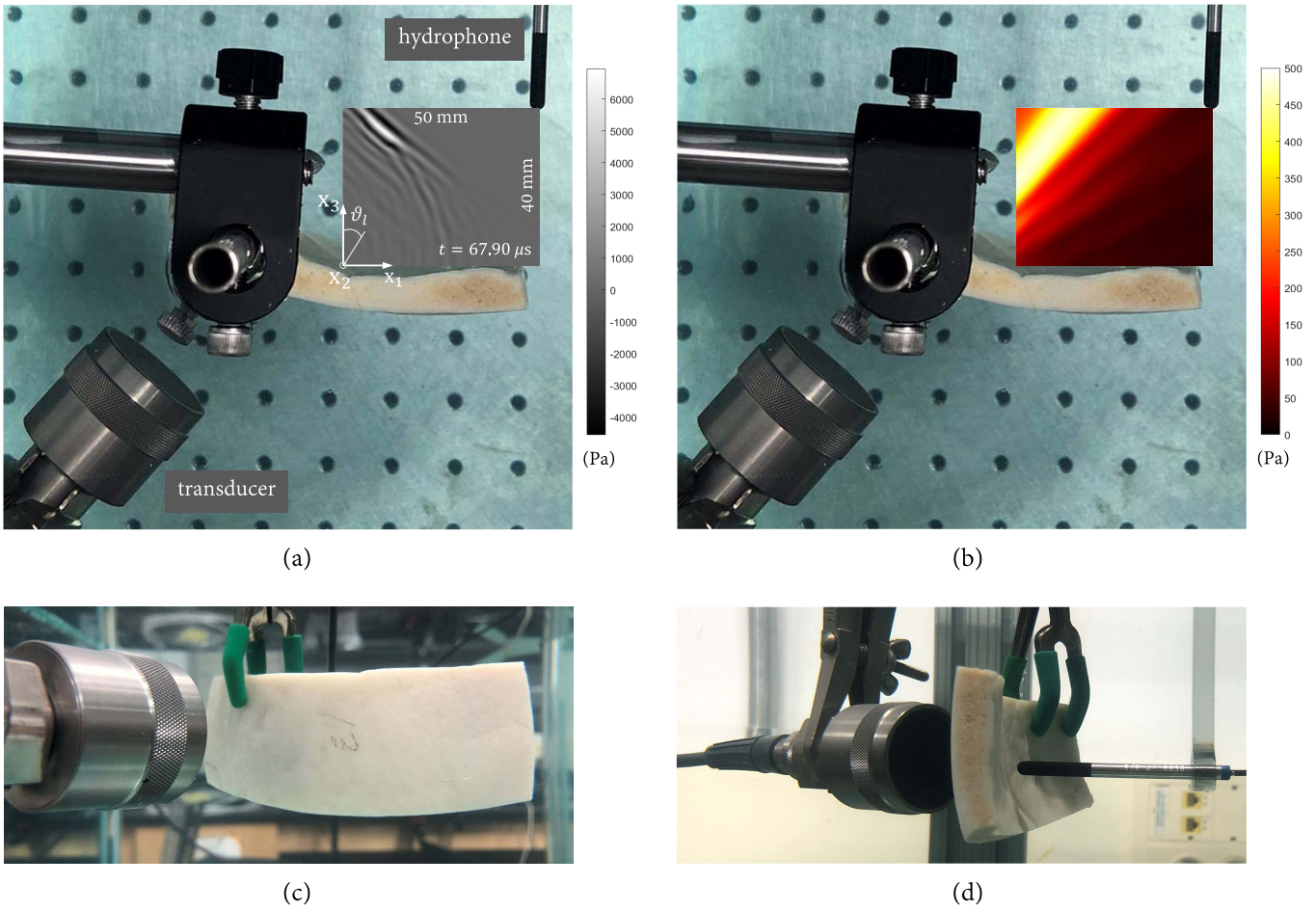

Fig. 9. Experimental setup for the parietal bone cut of Fig. 2(c). (a) Scan area and snapshot of the pressure field $p(t, x_1, x_3)$ at 67.90 μs. (b) RMS plot of the pressure field. (c) and (d) Lateral views.

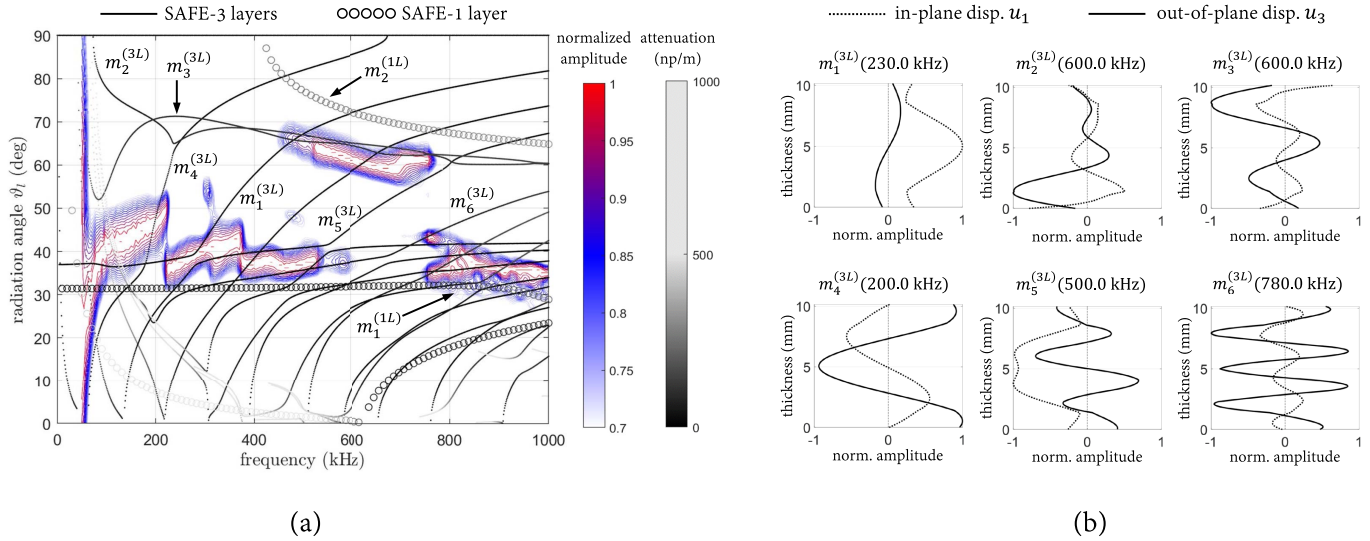

Fig. 10. (a) Experimental radiation angle dispersion diagram with superimposed SAFE dispersion curves for the three- and one-layer plate models. (b) In-plane and out-of-plane normalized displacements profiles for the guided wave modes $m_i^{(3L)}$, $i = 1, \ldots, 6$, at frequencies corresponding to the experimental dispersion branches.

sub-300 kHz range, the radiation is dominated by Lamb modes (the $m_1^{(3L)}$ and $m_1^{(1L)}$ modes, in particular), with a through-thickness displacement polarization that is dominant along the propagation direction (x_1-direction). This is also confirmed by experimental tests, which are presented in Section V for the parietal bone $s3$.

V. Experimental Validation

This section focuses on the experimental validation of the results obtained in Section IV-C2 for the parietal bone $s3$. The goal of the experimental validation is to compare the radiation angle dispersion diagrams obtained from immersed tests with those previously computed using FE time transient and SAFE analyses.

A. Experimental Setup and Data Acquisition

The experimental tests were performed for the degassed parietal bone of Fig. 2(c) using the underwater setup shown in Fig. 9. An ultrasonic immersion transducer (Olympus V391-SU, diameter: 28.58 mm, center frequency: 0.47 MHz, peak frequency: 0.46 MHz, and -6 dB bandwidth: 61.47%) was placed at a distance of 37 mm from the outer cortical table, facing it perpendicularly. The transducer was excited with a two-and-a-half cycle tone burst of 500 kHz center frequency using an arbitrary signal generator (HP 33120A) and a piezoelectric amplifier (Khron-Hite 7500). A needle hydrophone with flat frequency response (Teledyne Reson TC 4038, diameter: 4 mm, receiving sensitivity: 50–800 kHz, and nominal receiving sensitivity: -226 ± 3 dB re 1V/μPa at 500 kHz), placed at mid-width of the bone and connected through a preamplifier (Stanford Research Systems SR560) to a digital oscilloscope (HandyScope HS3), was used to record the pressure transmitted through the skull segment at a 10 MHz sampling rate using three averages per scan. The hydrophone was attached to a servomotor-operated stage that allows for precise position control via LabVIEW. The stage was programed to scan a rectangular area of dimensions 40 mm $\times$ 50 mm with a 0.25 mm step in each direction. At the scan points closest to the bone, the hydrophone was 3 mm away from the inner cortical table. The data were recorded for 250 μs such that the complete transmitted pressure signal is captured at all scan points. A snapshot of the recorded pressure field $p(t, x_1, x_3)$ is reported in Fig. 9(a) at $t = 67.90$ μs, where the separation between the transmitted and radiated leaky waves can be clearly observed. The difference between the energy carried by these waves can be observed from the root mean square (rms) plot of the pressure field, which is shown in Fig. 9(b). In general, it can be inferred that the acoustic energy associated with the direct wave is an order of magnitude larger than that of the radiated leaky waves. Finally, it is noted that the effects of diffraction from the edges of the skull specimen are negligible due to the fact that the 2-D pressure scan is obtained on a plane orthogonal to the bone surface and passing through the axis of symmetry of the skull sample. In addition, diffracted waves propagate in the surrounding fluid with semi-circular wavefronts, and therefore, their amplitude attenuates rapidly due to geometrical spreading. Thus, for a given guided wave mode, the magnitude of the diffracted wavefront that starts from the edge of the skull sample and reaches the scan plane is significantly lower than that of the leaky wave.

B. Results and Discussion

The experimental radiation angle dispersion diagram obtained using the setup of Fig. 9 and the procedure outlined in Section IV-B is reported in Fig. 10(a). In addition, the normalized in-plane and out-of-plane displacement profiles are shown in Fig. 10(b) for the guided wave modes $m_i^{(3L)}$, $i = 1, \ldots, 6$, at frequencies corresponding to the experimental dispersion branches. By comparison with the numerically computed diagram of Fig. 8, it can be inferred that the distribution of the radiated energy in terms of leakage angles is similar to that obtained from the FE analysis. Consequently, the experimental results also confirm the validity of the three-layer SAFE modeling approach.

Compared to the diagram of Fig. 8(b), in the experimental spectrum, the energy leaked at low frequencies extends beyond the fundamental mode $m_1^{(3L)}$ to include the mode $m_5^{(3L)}$ up to 500 kHz. This aspect can be related to the different sources used in the FE simulations and the experimental setup to excite the cranial bone. The slower branch observed from the FE analysis in the 300–850 kHz and $\vartheta_l \in [60, 70]^\circ$ ranges is also found in the experimental spectrum, although only limited to the 500–750 kHz range. As previously discussed, this branch is formed by the group of modes $m_3^{(3L)}$ and $m_4^{(3L)}$. The last branch present in the experimental spectrum is located in the 750–1000 kHz range and corresponds to a mean radiation angle $\vartheta_l \approx 35^\circ$. It is noted that this branch, which was not observed in the FE calculations, follows more closely the fast fundamental mode $m_1^{(1L)}$ predicted by the one-layer SAFE model. This behavior can potentially indicate a transition stage in which the mechanical energy in the bone progressively focuses in the proximity of the cortical layers with increasing frequency, i.e., decreasing wavelengths. Such phenomenon was experimentally observed by Estrada *et al.* [7] for quasi-Rayleigh waves and thickness-to-wavelength ratios in the range 3.5–6.3. For comparison, the wavelengths $\lambda(f)$ associated with this branch can be estimated from (2) by applying the fundamental relation $\lambda = 2\pi/k$, leading to $\lambda(f) = c_f/(f \sin(\vartheta_l))$. By substituting $\vartheta_l = 35^\circ$ in the previous equation, one finds $\lambda(f = 800\ \text{kHz}) = 3.2$ mm and $\lambda(f = 1.0\ \text{MHz}) = 2.6$ mm, which, in turn, corresponds to a thickness-to-wavelength ratio equal to 3.1 and 3.9, respectively.

VI. Conclusion

The radiation characteristics of cranial Lamb waves are investigated in the sub-1.0 MHz frequency range via SAFE models and time transient simulations performed on bone phantoms and real parietal geometries obtained from μCT scans. A key result of this study is to show that the frequency-dependent radiation angles of cranial leaky Lamb waves can be predicted by an equivalent three-layered waveguide model of the cranial bone. This is confirmed by means of time transient simulations on high fidelity models that leverage CT scan geometries of sections of the skull. The near-field pressure analyzed in terms of frequency-dependent radiation angles also indicates that, at frequencies lower than 300 kHz, fast Lamb modes with low radiation angles and prevalent in-plane displacement polarization dominate the radiation process. For slower modes with higher radiation angles and prevalent out-of-plane displacement polarization, the range of angles at

which energy flows from the bone to the fluid becomes larger due to the continuously changing cortical thickness and local characteristics such as diploë pores and discontinuities of the cortical layers, which translates into more irregular, and hard to predict, radiation branches. Finally, the results obtained from the numerical analyses of a parietal bone with a dense trabecular network have been confirmed experimentally by performing near-field pressure measurements in an immersed setup.

The understanding of the radiation properties of guided waves can support the development of novel strategies for brain imaging, diagnostics, and therapy. For example, in transcranial ultrasound imaging, guided waves could be employed as part of reconstruction algorithms, which strongly rely on the knowledge of the transmission and reflection properties of the cranial bone and on the ability to temporally separate bulk wave reflections in signals containing several wave signatures. Leaky and nonleaky guided waves can also be a viable tool for near-field imaging of the shallow brain cortex. Finally, the inherent ability to propagate over extensive portions of the cranial vault makes guided waves attractive for the characterization of the cranial bone marrow, which is diffusely distributed within the diploë. In this sense, guided waves could lead to the development of harmless substitutes to MRI and CT scan-based techniques in monitoring the development of systemic disorders.

Appendix
Mathematical Derivation of the Dispersion Equation

The dispersion equation of the SAFE model can be obtained from the application of a standard Galerkin procedure and results in an eigenvalue problem of the form

$$\left[k_1^2\mathbf{K}_3 + \mathrm{i}k_1\left(\mathbf{K}_2 - \mathbf{K}_2^{\mathrm{T}}\right) + \mathbf{K}_1 - (2\pi f)^2\mathbf{M} + Z(f,k_1)\mathbf{H}\right]\mathbf{U} = \mathbf{0} \tag{3}$$

where $Z(f,k_1) = 2\mathrm{i}\pi f\rho_f/k_3(f,k_1)$ represents the radiation impedance of an infinite plate [35], and $k_3(f,k_1) = [k_f^2(f) - k_1(f)^2]^{1/2}$ denotes the transverse wavenumber in the fluid half-space (see Fig. 3(c)), while the different stiffness and mass matrix operators are defined as

$$\mathbf{K}_1 = \mathop{\mathbf{A}}_{e=1}^{n} \int_{l_e} \left(\boldsymbol{\partial}_{x_3}\mathbf{N}(x_3)\right)^{\mathrm{T}}\mathbf{C}(x_3)\boldsymbol{\partial}_{x_3}\mathbf{N}(x_3)dx_3 \tag{4}$$

$$\mathbf{K}_2 = \mathop{\mathbf{A}}_{e=1}^{n} \int_{l_e} \left(\boldsymbol{\partial}_{x_3}\mathbf{N}(x_3)\right)^{\mathrm{T}}\mathbf{C}(x_3)\boldsymbol{\partial}_{\phi}\mathbf{N}(x_3)dx_3 \tag{5}$$

$$\mathbf{K}_3 = \mathop{\mathbf{A}}_{e=1}^{n} \int_{l_e} \left(\boldsymbol{\partial}_{\phi}\mathbf{N}(x_3)\right)^{\mathrm{T}}\mathbf{C}(x_3)\boldsymbol{\partial}_{\phi}\mathbf{N}(x_3)dx_3 \tag{6}$$

$$\mathbf{M} = \mathop{\mathbf{A}}_{e=1}^{n} \int_{l_e} \mathbf{N}^{\mathrm{T}}(x_3)\rho(x_3)\mathbf{N}(x_3)dx_3 \tag{7}$$

in which $\mathop{\mathbf{A}}_{e=1}^{n}$ indicates a matrix assembly operation in the direct stiffness sense, n is the total number of FEs in the mesh, $\mathbf{N}(x_3)$ is a 3×9 matrix of polynomial shape functions, and $\rho(x_3)$ and $\mathbf{C}(x_3)$ denote the density and fourth-order tensor of elastic moduli of the cortical bone, respectively, while

$$\boldsymbol{\partial}_{x_3} = \begin{bmatrix} 0 & 0 & 0 \\ 0 & 0 & 0 \\ 0 & 0 & \dfrac{\partial}{\partial x_3} \\ 0 & \dfrac{\partial}{\partial x_3} & 0 \\ \dfrac{\partial}{\partial x_3} & 0 & 0 \\ 0 & 0 & 0 \end{bmatrix}, \quad \boldsymbol{\partial}_{\phi} = \begin{bmatrix} 1 & 0 & 0 \\ 0 & 0 & 0 \\ 0 & 0 & 0 \\ 0 & 0 & 0 \\ 0 & 0 & 1 \\ 0 & 1 & 0 \end{bmatrix} \tag{8}$$

are compatibility operators. The operator $\mathbf{H}$ in (3) is a nodal collocation matrix for the displacement component u_3 at the solid-fluid interface.

Equation (3) corresponds to an ill-posed nonlinear eigenvalue system in which, due to the presence of the term $k_3(f,k_1)$, the matrix of coefficients becomes a dual-valued operator for any given set of solutions $(f,k_1(f))$. As shown by Mazzotti *et al.* [36], [37], the eigensolutions corresponding to leaky and nonleaky modes can be located on the physically admissible Riemann sheets by performing a contour integration on the plane $(\mathrm{Re}(k_1(f)), \mathrm{Im}(k_1(f)))$ and selecting the appropriate sign of $k_3(k)$ by enforcing the generalized Snell's law at each point of the contour path. However, Kiefer *et al.* [38] have demonstrated that a well-posed solution can be found by applying a trigonometric change of variables and converting the nonlinear eigenvalue problem to a linear one. By introducing the transformation $k_1(\gamma) = k_f(\gamma + \gamma^{-1})/2$, the transverse wavenumber in the fluid (see Fig. 3(c)) becomes $k_3(\gamma) = k_f(\gamma - \gamma^{-1})/(2i)$. Substituting $k_1(\gamma)$ and $k_3(\gamma)$ into (3) leads to the eigenequation (1), where the different matrix operators $\mathbf{A}_i$ $(i = 0, \ldots, 6)$ are expressed as

$$\mathbf{A}_0(f) = ik_f^3(f)\mathbf{K}_3 \tag{9}$$

$$\mathbf{A}_1(f) = -2\,k_f^2(f)\left(\mathbf{K}_2 - \mathbf{K}_2^{\mathrm{T}}\right) \tag{10}$$

$$\mathbf{A}_2(f) = ik_f^3(f)\mathbf{K}_3 + 4ik_f(f)\left(\mathbf{K}_1 - \pi^2 f^2\mathbf{M}\right) \tag{11}$$

$$\mathbf{A}_3(f) = 32i\pi^2 f^2\rho_f\mathbf{Q} \tag{12}$$

$$\mathbf{A}_4(f) = -ik_f^3(f)\mathbf{K}_3 - 4ik_f(f)\left(\mathbf{K}_1 - \pi^2 f^2\mathbf{M}\right) \tag{13}$$

$$\mathbf{A}_5(f) = 2\,k_f^2(f)\left(\mathbf{K}_2 - \mathbf{K}_2^{\mathrm{T}}\right) \tag{14}$$

$$\mathbf{A}_6(f) = -ik_f^3(f)\mathbf{K}_3. \tag{15}$$

References

[1] W. J. Tyler, "Noninvasive neuromodulation with ultrasound? A continuum mechanics hypothesis," *Neuroscientist*, vol. 17, no. 1, pp. 25–36, Feb. 2011.

[2] W. J. Elias *et al.*, "A randomized trial of focused ultrasound thalamotomy for essential tremor," *New England J. Med.*, vol. 375, no. 8, pp. 730–739, 2016.

[3] K. Hynynen *et al.*, "500-element ultrasound phased array system for noninvasive focal surgery of the brain: A preliminary rabbit study with *ex vivo* human skulls," *Magn. Reson. Med.*, vol. 52, no. 1, pp. 100–107, 2004.

[4] J. K. Mueller, L. Ai, P. Bansal, and W. Legon, "Computational exploration of wave propagation and heating from transcranial focused ultrasound for neuromodulation," *J. Neural Eng.*, vol. 13, no. 5, Jul. 2016, Art. no. 056002.

[5] V. Ozenne *et al.*, "MRI monitoring of temperature and displacement for transcranial focus ultrasound applications," *NeuroImage*, vol. 204, Jan. 2020, Art. no. 116236.

[6] H. Estrada, J. Rebling, and D. Razansky, "Prediction and near-field observation of skull-guided acoustic waves," *Phys. Med. Biol.*, vol. 62, no. 12, pp. 4728–4740, May 2017.
[7] H. Estrada, S. Gottschalk, M. Reiss, V. Neuschmelting, R. Goldbrunner, and D. Razansky, "Observation of guided acoustic waves in a human skull," *Ultrasound Med. Biol.*, vol. 44, no. 11, pp. 2388–2392, Nov. 2018.
[8] H. Estrada *et al.*, "Looking at the skull in a new light: Rayleigh-Lamb waves in cranial bone," in *Proc. IEEE Int. Ultrason. Symp. (IUS)*, Oct. 2018, pp. 1–3.
[9] C. Sugino, M. Ruzzene, and A. Erturk, "Experimental and computational investigation of guided waves in a human skull," *Ultrasound Med. Biol.*, vol. 47, no. 3, pp. 787–798, Mar. 2021.
[10] K. Firouzi, P. Ghanouni, and B. T. Khuri-Yakub, "Efficient transcranial ultrasound delivery via excitation of Lamb waves: Concept and preliminary results," in *Proc. IEEE Int. Ultrason. Symp. (IUS)*, Sep. 2017, pp. 1–4.
[11] K. C. Kang, Y. H. Kim, K. K. Park, K. Firouzi, and P. Khuri-Yakub, "Transcranial ultrasound delivery using dual-mode conversion," in *Proc. 7th Int. Symp. Focused Ultrasound (IEEE)*, 2020.
[12] C. Adams, J. McLaughlan, L. Nie, and S. Freear, "Excitation and acquisition of cranial guided waves using a concave array transducer," in *Proc. Meetings Acoust. 173EAA*, 2017, vol. 30, no. 1, Art. no. 055003.
[13] J.-F. Aubry, M. Tanter, M. Pernot, J.-L. Thomas, and M. Fink, "Experimental demonstration of noninvasive transskull adaptive focusing based on prior computed tomography scans," *J. Acoust. Soc. Amer.*, vol. 113, no. 1, pp. 84–93, Jan. 2003.
[14] G. Luo *et al.*, "Computational methods for ultrasonic bone assessment," *Ultrasound Med. Biol.*, vol. 25, no. 5, pp. 823–830, Jun. 1999.
[15] A. Hosokawa, "Simulation of ultrasound propagation through bovine cancellous bone using elastic and Biot's finite-difference time-domain methods," *J. Acoust. Soc. Amer.*, vol. 118, no. 3, pp. 1782–1789, 2005.
[16] A. Hosokawa, "Ultrasonic pulse waves in cancellous bone analyzed by finite-difference time-domain methods," *Ultrasonics*, vol. 44, pp. e227–e231, Dec. 2006.
[17] Y. Nagatani, H. Imaizumi, T. Fukuda, M. Matsukawa, Y. Watanabe, and T. Otani, "Applicability of finite-difference time-domain method to simulation of wave propagation in cancellous bone," *Jpn. J. Appl. Phys.*, vol. 45, no. 9A, pp. 7186–7190, Sep. 2006.
[18] Y. Nagatani, K. Mizuno, T. Saeki, M. Matsukawa, T. Sakaguchi, and H. Hosoi, "Numerical and experimental study on the wave attenuation in bone—FDTD simulation of ultrasound propagation in cancellous bone," *Ultrasonics*, vol. 48, no. 6, pp. 607–612, 2008.
[19] A. Hosokawa, "Development of a numerical cancellous bone model for finite-difference time-domain simulations of ultrasound propagation," *IEEE Trans. Ultrason., Ferroelectr., Freq. Control*, vol. 55, no. 6, pp. 1219–1233, Jun. 2008.
[20] A. S. Aula, J. Töyräs, M. A. Hakulinen, and J. S. Jurvelin, "Effect of bone marrow on acoustic properties of trabecular bone–3D finite difference modeling study," *Ultrasound Med. Biol.*, vol. 35, no. 2, pp. 308–318, Feb. 2009.
[21] P. Laugier and G. Haïat, *Bone Quantitative Ultrasound*, vol. 576. Dordrecht, The Netherlands: Springer, 2011.
[22] L. Goossens *et al.*, "The correlation between the SOS in trabecular bone and stiffness and density studied by finite-element analysis," *IEEE Trans. Ultrason., Ferroelectr., Freq. Control*, vol. 55, no. 6, pp. 1234–1242, Jun. 2008.
[23] G. Pinton, M. Pernot, E. Bossy, J.-F. Aubry, M. Muller, and M. Tanter, "Mechanisms of attenuation and heating dissipation of ultrasound in the skull bone: Comparison between simulation models and experiments," in *Proc. IEEE Int. Ultrason. Symp.*, Oct. 2010, pp. 225–228.
[24] G. Pinton, J.-F. Aubry, E. Bossy, M. Muller, M. Pernot, and M. Tanter, "Attenuation, scattering, and absorption of ultrasound in the skull bone," *Med. Phys.*, vol. 39, no. 1, pp. 299–307, Dec. 2011.
[25] X. Chou, F. Xu, Y. Li, C. Liu, D. Ta, and L. H. Le, "Variability in ultrasound backscatter induced by trabecular microstructure deterioration in cancellous bone," *BioMed Res. Int.*, vol. 2018, pp. 1–7, Jan. 2018.
[26] *Materialise Mimics*. [Online]. Available: https://www.materialise.com/en/medical/mimics-innovation-suite/mimics
[27] J. Peterson and P. C. Dechow, "Material properties of the human cranial vault and zygoma," *Anatomical Rec. A, Discoveries Mol., Cellular, Evol. Biol.*, vol. 274A, no. 1, pp. 785–797, 2003.
[28] E. Kohtanen, M. Mazzotti, M. Ruzzene, and A. Erturk, "Vibration-based elastic parameter identification of the diploë and cortical tables in dry cranial bones," *J. Mech. Behav. Biomed. Mater.*, 2021.
[29] I. Bartoli, A. Marzani, F. L. di Scalea, and E. Viola, "Modeling wave propagation in damped waveguides of arbitrary cross-section," *J. Sound Vib.*, vol. 295, nos. 3–5, pp. 685–707, Aug. 2006.
[30] M. Mazzotti, A. Marzani, I. Bartoli, and E. Viola, "Guided waves dispersion analysis for prestressed viscoelastic waveguides by means of the SAFE method," *Int. J. Solids Struct.*, vol. 49, no. 18, pp. 2359–2372, Sep. 2012.
[31] T. Hayashi and D. Inoue, "Calculation of leaky Lamb waves with a semi-analytical finite element method," *Ultrasonics*, vol. 54, no. 6, pp. 1460–1469, Aug. 2014.
[32] J. Gao *et al.*, "A free plate model could predict ultrasonic guided waves propagation in a 3D printed skull phantom," in *Proc. IEEE Int. Ultrason. Symp. (IUS)*, Oct. 2019, pp. 2031–2033.
[33] *Comsol Multiphysics 5.4*. [Online]. Available: https://www.comsol.com/
[34] M. Mazzotti, C. Sugino, E. Kohtanen, A. Erturk, and M. Ruzzene, "Experimental identification of high order Lamb waves and estimation of the mechanical properties of a dry human skull," *Ultrasonics*, vol. 113, May 2021, Art. no. 106343.
[35] F. Fahy and P. Gardonio, *Sound and Structural Vibration*, 2nd ed. Oxford, U.K.: Elsevier, 2007.
[36] M. Mazzotti, I. Bartoli, A. Marzani, and E. Viola, "A coupled SAFE-2.5D BEM approach for the dispersion analysis of damped leaky guided waves in embedded waveguides of arbitrary cross-section," *Ultrasonics*, vol. 53, no. 7, pp. 1227–1241, Sep. 2013.
[37] M. Mazzotti, I. Bartoli, and A. Marzani, "Ultrasonic leaky guided waves in fluid-coupled generic waveguides: Hybrid finite-boundary element dispersion analysis and experimental validation," *J. Appl. Phys.*, vol. 115, no. 14, Apr. 2014, Art. no. 143512.
[38] D. A. Kiefer, M. Ponschab, S. J. Rupitsch, and M. Mayle, "Calculating the full leaky Lamb wave spectrum with exact fluid interaction," *J. Acoust. Soc. Amer.*, vol. 145, no. 6, pp. 3341–3350, Jun. 2019.

Matteo Mazzotti received the Ph.D. degree in structural engineering from the University of Bologna in 2013. He is currently a Research Associate with the Department of Mechanical Engineering, University of Colorado Boulder, where he performs research on the dynamics of the human skull, biosensors, metamaterials, composite structures, and magnetostrictive actuators. He has authored several publications in the fields of non-destructive evaluation, structural health monitoring, numerical methods for solid and fluid dynamics, and optimization problems.

Eetu Kohtanen received the B.S. degree in mechanical engineering and the M.S. degree in engineering from the University of Georgia, in 2017 and 2019, respectively. He is currently pursuing the Ph.D. degree in mechanical engineering degree with the Georgia Institute of Technology. His present research interests include the structural mechanics of the human skull and its higher frequency wave propagation characteristics.

Alper Erturk received the Ph.D. degree in engineering mechanics from Virginia Tech in 2009.

He is currently the Woodruff Professor with the G. W. Woodruff School of Mechanical Engineering, Georgia Institute of Technology, Atlanta, GA, USA, where he leads the Smart Structures and Dynamical Systems Laboratory. He has published two books and more than 200 papers in journals and conference proceedings on topics spanning from vibration energy harvesting and bioinspired actuation to elastic/acoustic metamaterials and phononic crystals.

Dr. Erturk is a fellow of the American Society of Mechanical Engineers (ASME) and The International Society for Optics and Photonics (SPIE). He is a recipient of various awards, including an NSF CAREER Award (2013), an ASME Gary Anderson Early Achievement Award (2015), an ASME C.D. Mote Jr. Early Career Award (2017), and an SEM J.W. Dally Young Investigator Award (2020), among others.

Massimo Ruzzene received the Ph.D. degree in applied mechanics from the Politecnico di Torino, Italy, in 1999.

He is currently the Slade Professor of Mechanical Engineering and holds a joint appointment in the Smead Aerospace Engineering Sciences Department of CU Boulder. He joined CU in the Summer of 2019, after serving as the Pratt and Whitney Professor with the Schools of Aerospace and Mechanical Engineering, Georgia Institute of Technology. He is the author of two books, more than 190 journal papers, and 280 conference papers. His current and past research has focused on solid mechanics, structural dynamics, and wave propagation, with applications to ultrasonic imaging, structural health monitoring, metamaterials, and vibration and noise control.

Dr. Ruzzene is a fellow of the American Society of Mechanical Engineers (ASME) and the Society of Engineering Science (SES). He is also an Associate Fellow of the American Institute of Aeronautics and Astronautices (AIAA).